



Low temperature upgrading glucose to aromatics via a H₂-free melting-catalysis strategy

Zhe Zhang^{a,1}, Huan Chen^{a,1}, Helin Pan^a, Dengle Duan^{c,*}, Yayun Zhang^{a,b,**}, Donghui Long^{a,b}

^a Key Laboratory of Chemical Engineering, East China University of Science and Technology, Shanghai 200237, China

^b Key Laboratory of Specially Functional Polymeric Materials and Related Technology (Ministry of Education), School of Chemical Engineering, East China University of Science and Technology, Shanghai 200237, China

^c Guangdong Provincial Key Laboratory of Lingnan Specialty Food Science and Technology, Zhongkai University of Agriculture and Engineering, Guangzhou, 510000, China

ARTICLE INFO

Keywords:

Low temperature
Glucose conversion
Mesoporous ZSM-5
Aromatics
Acidity

ABSTRACT

Converting biomass into valuable aromatics is a desirable way to alleviate global energy crisis but is currently challenged by massive energy consumption. Herein, a H₂-free melting-catalysis strategy is proposed for direct converting glucose into aromatics under mild conditions by nano-sized mesoporous ZSM-5. We demonstrate that the melting of glucose promotes the accessibility to catalytic sites and enhances subsequent catalytic processes. The introduction of inter-crystalline mesopores facilitates diffusion of molecules, and the moderate acidity favors the deoxygenation of oxygenated intermediates, both of which promote aromatics formation. Consequently, 10-ZSM-5-80 with abundant inter-crystalline mesopores and optimum acidity achieves a maximum aromatics selectivity of 95.4 area% at 280 °C, of which 70.2% are monocyclic aromatic hydrocarbons. Furthermore, a possible mechanism is proposed based on experimental and online TG-FTIR-MS results. Our findings provide a new pathway for the selective generation of aromatics from glucose, which is expected to advance next-generation biomass utilization.

1. Introduction

Growing concerns about fossil fuel shortages and global warming have necessitated the search for alternative sustainable energy sources. As the sole renewable carbon resource on Earth, biomass has attracted significant attention [1]. Biomass is globally available, and approximately 1700 billion tons of biomass is produced annually, which is equivalent to 850 billion tons of standard coal or 600 billion tons of oil equivalents [2]. However, only ~5% of the biomass is currently being used, and if all available biomass is converted into biofuels, it may significantly alleviate the energy crisis. Several countries have passed legislation mandating increased use of renewable biofuels. For instance, the U.S. Department of Agriculture (USDA) and Department of Energy (DOE) have set ambitious targets to replace 20% of transportation energy and 25% of chemical commodities with biofuel-based alternatives by 2030 [3]. These goals have contributed to an intensified interest in developing biomass valorization technique to achieve carbon neutrality.

Thermochemical conversion has been considered as an efficient way to convert biomass into liquid fuels and value-added aromatic chemicals among the available technologies [4,5]. Thermochemical conversion technologies such as fast pyrolysis enables biomass feedstock transformation into bio-oil (including furfurals, acids, hydrocarbons etc.) [6]. However, efforts in this method have met with limited success, as excess oxygen-containing functional groups (30–50 wt%) result in pyrolysis oil with low calorific value of combustion and thermal stability, as well as high viscosity and corrosiveness. In contrast, catalytic fast pyrolysis (CFP), which directly integrates fast biomass pyrolysis and catalytic bio-oil upgrading, overcomes these limitations and has received increasing attention in improving bio-oil quality [7]. The initial attempt is to use solid acid catalysts (e.g., γ -Al₂O₃, H β , HY and ZSM-5) to selectively deoxidize bio-oils and convert the active oxygenates to chemically stable aromatic hydrocarbons through deoxygenation reactions including dehydration, decarbonylation and decarboxylation [8–10]. However, the energy-intensive CFP not only requires significant

* Corresponding author.

** Corresponding author at: Key Laboratory of Chemical Engineering, East China University of Science and Technology, Shanghai 200237, China.

E-mail addresses: duandengle@zhku.edu.cn (D. Duan), yy.zhang@ecust.edu.cn (Y. Zhang).

¹ These authors contributed equally to this work

energy consumption, but also lead to undesired light gas production and rapid catalyst deactivation due to thermodynamically oriented coke formation. Therefore, it is imperative to develop an energy-efficient biomass conversion technique that can produce high-quality biofuels and value-added aromatic chemicals to achieve economic viability.

Recently, extensive efforts have paid to catalytic conversion of biomass into valuable products under mild conditions. Advanced chemicals can be produced by aqueous-phase processing (APP) of biomass at low temperature of 100–300 °C. Whereas APP also has technical challenges and it is difficult to achieve efficient and highly selective production of aromatics in the reaction process [11–13]. Currently, the use of noble metal-based bifunctional catalysts in hydrogenation reactions can lower the reaction temperature to produce hydrocarbon fuels. A breakthrough has been achieved in the hydrogenolysis of lignin to advanced biofuels at 310 °C under 0.5 MPa H₂ for 40 h using deliberately designed Ru/NbOP₄ catalysts [14]. However, this method can merely obtain aromatics from lignin, which is rich in aromatic structures, while carbohydrates of largest content in biomass such as cellulose or its constituent unit glucose are not available. In addition, the scarcity of precious metals on Earth and the high cost of H₂ undermine the practicality of large-scale biomass processing. To date, thermochemical conversion of glucose to aromatic fuels under mild conditions (<300 °C, without H₂) has rarely been reported.

Herein, we reported a low-temperature, H₂-free melting-catalysis strategy for direct conversion of glucose into aromatics by rationally designed nano-sized mesoporous ZSM-5 catalyst (Fig. 1a). The abundant

inter-crystalline mesopores and moderate acidity of nano-sized ZSM-5 zeolite enhances mass transfer of molten glucose and intermediates, and subsequent products diffusion out of catalyst, thus achieving a maximum selectivity of 95.4 area% for aromatic hydrocarbons at 280 °C, with 70.2% of them being monocyclic aromatic hydrocarbons (MAHs, C₆–C₁₀). To the best of our knowledge, this is the first example of low-temperature conversion of glucose into aromatics in the absence of H₂, providing a novel route to the upgrading of renewable biomass.

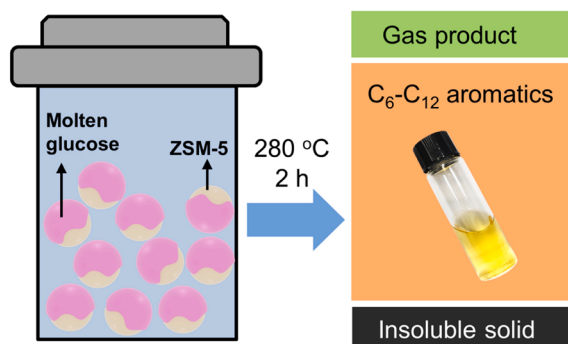
2. Experimental section

2.1. Chemicals and materials

Tetrapropylammonium hydroxide solution (TPAOH, 40 wt%, Shanghai Titan technology Co., Ltd), tetraethyl orthosilicate (TEOS, 99.9 wt%, Moen), aluminum isopropoxide (C₉H₂₁AlO₃, 99 wt%, Aladdin), ethyl acetate (C₄H₈O₂, 99.9%, Aladdin), D-glucose (C₆H₁₂O₆, 99%, Aladdin). All chemicals were used without further purification.

MCM-41 and SAPO-34 zeolite (Beijing HWRK Chem Co., Ltd), γ-Al₂O₃ (99.99% metal basis, Macklin), nanocellulose fiber (NCF, Shanghai Tonghua chem-Tech Co., Ltd.), standard gas (gas component is shown in Table S1, Shanghai Weichuang standard gas analysis technology Co., Ltd.). All catalysts were pretreated at 550 °C for 4 h prior to use to remove any impurities. Nanocellulose fiber was pre-dried at 80 °C overnight before use.

a Low-temperature melting strategy



b

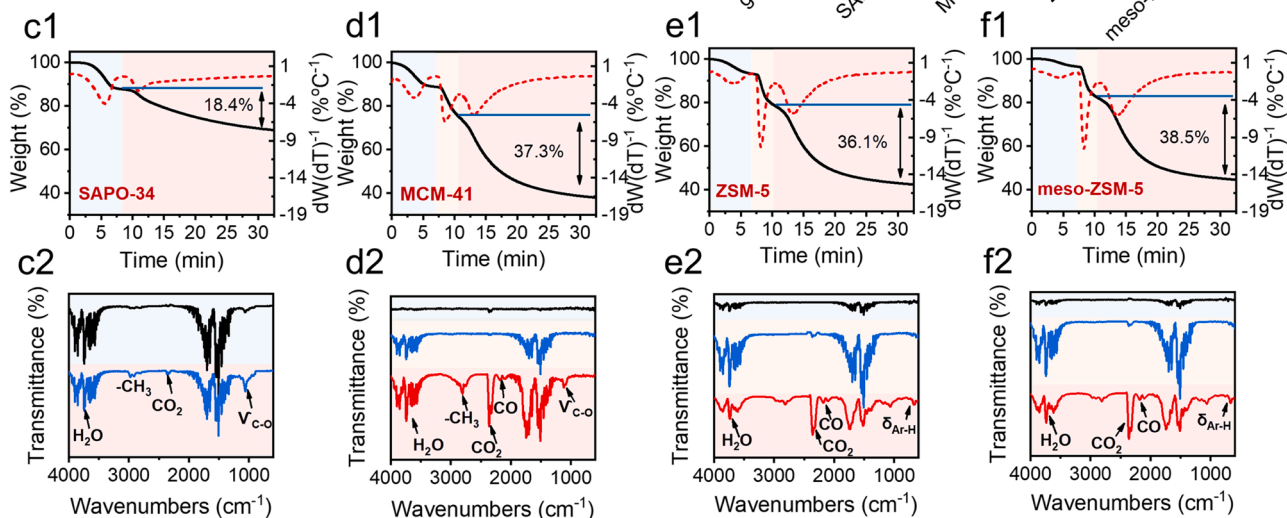
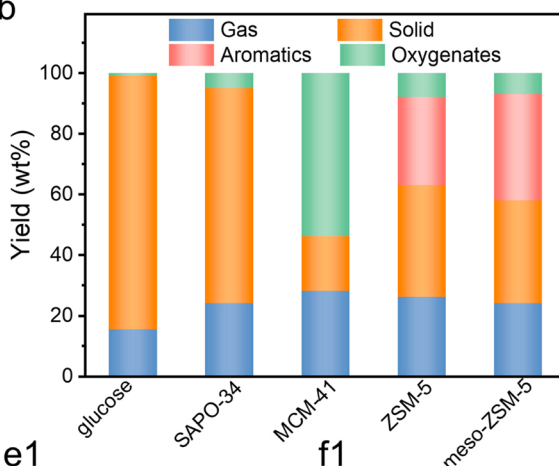


Fig. 1. (a) Schematic of the low temperature melting strategy for glucose conversion. (b) Product distributions over various solid catalysts. Reaction conditions: 1 g of catalyst, 0.5 g of glucose, 280 °C, 2 h. (c1–f1) TG and DGT profiles of the various catalysts in glucose conversion. (c2–f2) Corresponding FTIR spectra of the gaseous products at the maximum decomposition rate.

2.2. Catalyst preparation

ZSM-5 zeolites with different NCF content and Si/Al ratios were synthesized using a traditional hydrothermal method. In a typical synthesis (Fig. S1), 11.44 g of TPAOH solution and 0.23 g of 99 wt% $C_9H_{21}AlO_3$ were added to 32.4 g deionized water, and then 18.77 g of TEOS was added dropwise under stirring at room temperature for 2 h. The molar ratio of precursor was 1.0 SiO_2 : 0.25 TPAOH: 0.0125 Al_2O_3 : 20.0 H_2O . The resulting mixture was pre-crystallized at 80 °C for 12 h. Afterward, 0.54 g NCF was added to the above solution and sonicated for 30 min to make it evenly dispersed. The homogeneous white lotion was transferred into a 100 mL Teflon-lined stainless-steel autoclave and crystallized at 180 °C for 24 h. Finally, the solid precipitation was centrifuged, washed with deionized water several times, and then dried at 80 °C for 12 h. Removal of templates by calcination in air at 550 °C for 6 h produces white powders denoted as x -ZSM-5- y , where x refers to the mass percentage of NCF to SiO_2 , and y represents the Si/Al ratio.

2.3. Catalyst characterization

The phase structure of the samples was collected on a Bruker D8 Advance X-ray diffractometer with $Cu K_{\alpha}$ ($\lambda = 1.5406 \text{ \AA}$, 40 kV \times 40 mA) radiation over a 2θ range of 5–60° and a scanning speed of $10^\circ \text{ min}^{-1}$. The morphology and microstructure of the samples were observed by scanning electron microscopy (SEM, Nova NanoSEM-450) and transmission electron microscopy (TEM, JEM-2100). Due to the poor electrical conductivity of aluminosilicates, the samples were sprayed with gold prior to testing. The Si/Al ratios (SiO_2/Al_2O_3 , molecular ratios) of different samples were determined by inductively coupled plasma-optical emission spectroscopy (ICP-OES, Agilent 5110). N_2 adsorption-desorption experiments were performed on a Quadrasorb SI analyzer at 77 K. Before test, samples were degassed in vacuum at 474.15 K for 6 h to remove any moisture and impurities. The specific surface area (S_{BET}) and total pore volume (V_t) were calculated using the Brunauer–Emmett–Teller (BET) method and the single point method at the relative pressure of 0.985, respectively.

Acidity of the samples was measured by ammonia-temperature programmed desorption (NH_3 -TPD) on a AutoChem II 2920 instrument. Typically, 100 mg of the sample was pretreated with a helium stream at 300 °C for 1 h. After the sample was cool down to 50 °C, a NH_3 -He gas mixture (10 vol% NH_3) was purged into the chamber at a flow rate of 50 mL/min for 1 h until saturation. After removing the physically adsorbed NH_3 by flowing helium for 1 h, the sample was heated to 600 °C at a heating rate of 10 °C/min. The type of acid sites (Brønsted and Lewis acid sites) was determined by Fourier transform infrared spectroscopy of pyridine-adsorbed (Py-IR) on a Tensor 27 instrument. The samples were pretreated for 2 h at 350 °C under vacuum to remove the impurities, and then exposed to pyridine at room temperature until saturation. Finally, the infrared spectrum was recorded when the temperature dropped to 350 °C. ^{27}Al MAS NMR spectroscopy was performed using a BRUKER AVANCE NEO 400WB spectrometer.

Evolved gas analysis during the entire reaction process was conducted by a combination of thermogravimetric analysis (PerkinElmer TGA 4000), a Fourier-transform infrared analysis (FT-IR, PerkinElmer Spectrum Two) and mass spectrometry (MS, PerkinElmer SQ8), wherein the mixed samples of 2:1 of mass ratio of catalyst to glucose were heated from 30° to 280°C at a heating rate of 20 °C/min and then held for 20 min in N_2 flow. Thermogravimetry-differential scanning calorimetry (TG-DSC) was performed with a Germany-NETZSCH JUPITER F3 equipment with the same heating procedure as TGA.

2.4. Catalytic tests

The in-situ low-temperature glucose transformation experiments were conducted in a 50 mL stainless-steel autoclave connected to a mass flow controller and a condensation unit (Fig. S2). Note: The inlet and

outlet valves of the reactor are only opened at the end of the reaction. Before each reaction, glucose was dried at 80 °C for 6 h to remove any physically bound moisture. In a typical reaction, a well-mixed catalyst (1 g) and glucose (0.5 g) were loaded in the reactor. The system was initially swept by N_2 with a flow rate of 100 mL/min for 30 min to remove the inside air. Then the reactor was heated to 280 °C at a rate of 5 °C/min and held for another 2 h. After the reaction, the system was quenched to ambient temperature in an ice water bath. After opening the valves, the non-condensable vapors were driven to a 2 L gas sampling bag at the end of the system by N_2 and quantitatively analyzed on a gas chromatography (GC). The residual was extracted by 10 mL ethyl acetate and the insoluble material was filtered off, and then dried in a vacuum oven at 80 °C to volatilize the residual ethyl acetate on it. The ethyl acetate-soluble products were defined as the liquid oil and were analyzed by gas chromatography-mass spectrometry (GC-MS). The mass of liquid can be calculated from the mass difference of the material before and after the dissolution ethyl acetate. The solid products were mainly char and coke, which were referred to as the solid derived from glucose decomposition and the solid deposited on catalysts, respectively. The solid mass can be calculated from the mass difference of the catalyst before and after reaction. The detailed calculation method for product yields is shown below.

$$Y_{liquid} = \frac{M_{liquid}}{M_{glucose}} \times 100\%$$

$$Y_{solid} = \frac{M_{solid}}{M_{glucose}} \times 100\%$$

$$Y_{gas} = 100\% - (Y_{liquid} + Y_{solid})$$

Where Y_{liquid} , Y_{solid} , and Y_{gas} represent the yields of the liquid, solid, and gas products, respectively. M_{liquid} , M_{solid} , and $M_{glucose}$ denote the weight of each phase. Each experiment was performed there to four times to ensure the result reliability.

2.5. Gas and bio-oil characterization

The chemical composition of the gas and bio-oil were analyzed on an online gas chromatography (GC) and gas chromatography-mass spectrometry (GC-MS).

The condition of GC is as follow: Agilent GC 8860 equipped with an Alumina column (Agilent 115-3552, 50 m \times 530 μ m), a flame ionization detector (FID), and a thermal conductivity detector (TCD). The carrier gas is Argon with a flow rate of 1 mL/min. The temperature of FID and TCD are fixed at 300 and 250 °C, respectively. Temperature program starts with 60 °C isothermal for 5 min, heating from 60 to 180 °C with a ramping rate of 10 °C/min, and finally holding at 180 °C for 5 min

The condition of GC-MS is as follow: Agilent 6890 N/5975i equipped with a HP-5 capillary column (19091 J-433, 30 m \times 0.25 mm \times 0.25 μ m). The carrier gas is helium with a flow rate of 0.6 mL/min. The temperature of FID was fixed at 250 °C. Injection of 1 μ L sample with a split ratio of 20:1. Temperature program begins with 40 °C isothermal for 5 min, then heating from 40 to 280 °C at a ramping rate of 10 °C/min, and then holding at 280 °C for 5 min

Given that the chemical composition of bio-oil is complicated, the semi-quantitative chromatographic area percentage (area%) is used to calculate the selectivity for each compound as has been reported in our previous work [15]. Identification of resulting products is realized by comparing the spectral data with that from the NIST14 mass spectral library database. Any library-matched result with a match quality level lower than 80% is classified as “not identified” and rejected.

3. Results and discussion

3.1. Catalyst screening

Solid acid catalysts have been shown to be active for the cleavage of both C-C and C-O bonds in biomass [16,17]. In a proof-of-concept experiment, various solid acid catalysts, namely SAPO-34, MCM-41, and ZSM-5, were first screened for the conversion of glucose at 280 °C, and the corresponding product yields are shown in Fig. 1b. In the blank run without catalyst at 280 °C for 2 h, glucose mainly underwent a dehydration process to form amorphous carbon with almost undetectable bio-oil, as confirmed by the XRD and high intensity water signal from TG-IR (Fig. S3). In the reaction with SAPO-34, the yield of solid product reached 71%, and the resulting bio-oil was dominated with oxygenates and did not contain any aromatics (Fig. 1c) owing to the shape selectivity of small eight-ring pore opening ($d < 4.30 \text{ \AA}$) (Fig. S4) [2]. For large-pore MCM-41 zeolite, the liquid yield significantly increased to 54%. However, the weaker acidity limited their deoxygenation ability in to aromatics (Fig. S5) [18]. The liquid oil is mainly oxygenated bio-oil with poor thermal stability, which was confirmed by the C-O stretching vibration peak analyzed by IR (Fig. 1d, oil generation stage yield is 37.3%). In contrast, medium-pore ZSM-5 zeolite ($5.2 \text{ \AA} < d < 5.9 \text{ \AA}$) afforded a high aromatic yield of 29.1%, confirmed by the distinct aromatic vibrational peaks in FTIR. The outstanding performance of ZSM-5 zeolite for the selective production of aromatics correlates with its well-known five-membered ring channels [19]. However, the accessibility to inner acid sites for further reactions is greatly limited due to their large number of micropores. As a result, intermediates are prone to undergo secondary reactions on the external surface of ZSM-5, resulting in low yield in the oil generation stage

(36.1%, Fig. 1e) and severe coking (37%).

It has been reported that the introduction of mesopores in ZSM-5 could alleviate the diffusion limitations of macromolecules and promote the utilization of internal acidic sites thereby facilitating the conversion of intermediates [20,21]. Interestingly, we find that ZSM-5 zeolite with deliberately introduced inter-crystalline mesopores by nanocellulose fiber (NCF) modification could significantly boost the catalysis, giving an aromatic yield of at 35% (Fig. 1b). Meanwhile, TG-IR analysis exhibits distinct aromatic vibrational peaks (Fig. 1f), indicating a superior selectivity. Therefore, conversion glucose into aromatics under mild conditions rely on the catalyst with abundant mesopores and moderate acidity. Therefore, nano-sized mesoporous ZSM-5 zeolite with various Si/Al ratios were synthesized for further experiment.

3.2. Characterization of the catalysts

The morphology and pore structure of the NCF-modified catalysts were investigated by SEM and TEM. 0-ZSM-5-80 exhibits a smooth crystalline surface (Fig. 2a) and no evident bright spots corresponding to the mesopores are observed (Fig. 2e). In contrast, NCF-modified zeolites form loosely packed crystal assembly and show bright spots, suggesting the formation of inter-crystal voids [22]. Meanwhile, the introduction of NCF not only induced the formation of mesopores, but also well preserve the microporous structure, forming a hierarchical structure of ZSM-5 zeolite. However, the hierarchical structures of 5-ZSM-5-80 and 20-ZSM-5-80 are less pronounced compared with the 10-ZSM-5-80 (Fig. 2b-d, f-h), which can be explained by the poor dispersion of a small amount of NCF in the Si-Al precursor solution, while an excess of NCF tends to agglomerate (Fig. S6) and reduce the template effect. Therefore, reasonable control of NCF addition is essential for the preparation of

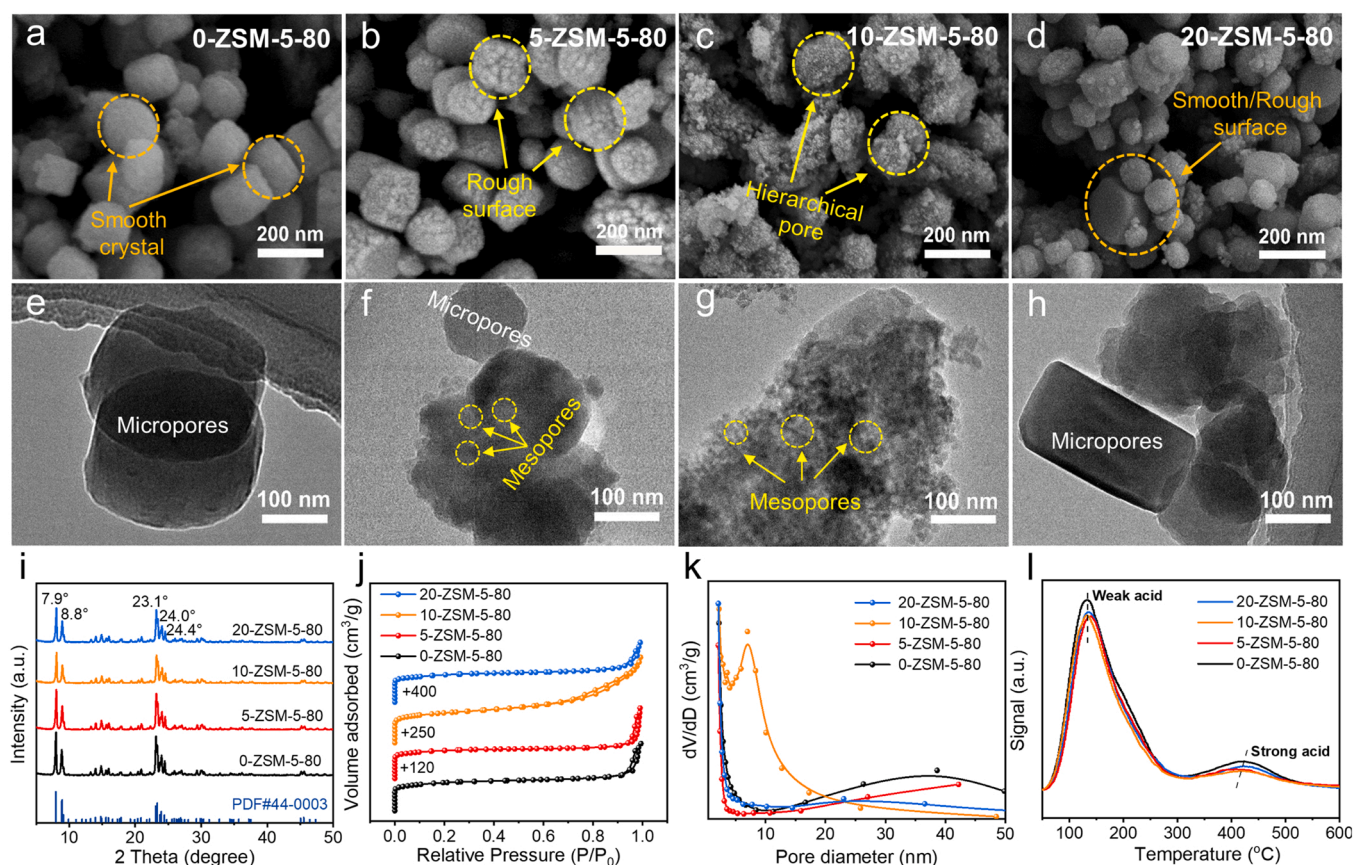


Fig. 2. Characterization of x-ZSM-5-80 zeolites with varied NCF-additions (a-d) SEM images of (a) ZSM-5-80, (b) 5-ZSM-5-80, (c) 10-ZSM-5-80, (d) 20-ZSM-5-80. (e-h) TEM images of (e) ZSM-5-80, (f) 5-ZSM-5-80, (g) 10-ZSM-5-80, (h) 20-ZSM-5-80. (i) XRD patterns. (j-k) N₂ adsorption-desorption isotherms and pore size distribution. (l) NH₃-TPD isotherms.

zeolites with different pore structures.

The powder XRD patterns of the zeolites prepared under different conditions are shown in Fig. 2i and Fig. S7. As can be seen that all samples exhibit well-resolved “five-finger” peaks ($2\theta = 7.9, 8.8, 23.1, 24.0$ and 24.4°) of ZSM-5 with undetectable impurities, in agreement with the typical pattern of MFI crystalline structure (JCPDS No. 44-0003) [23], confirming the successful synthesis of ZSM-5 with different NCF additions (0, 5, 10 and 20) and different Si/Al ratios (40, 80, 100 and 150). A decreased peak intensity is observed for 10-ZSM-5-80 (Fig. 2i), probably due to more framework defects exposed on the external surface as the crystal size decrease [22]. In addition, a weaker intensity of the characteristic peaks is observed with the increasing Al content (Fig. S7), which is due to the replacement of Si atoms by larger Al atoms, resulting in an increase in the unit cell volume [24].

The porosity of ZSM-5 series is further analyzed by N_2 sorption. As shown in Fig. 2j-k, the sharp N_2 uptake in the low relative pressure region ($P/P_0 < 0.001$) for all samples indicate that the typical microporous nature of ZSM-5 zeolite is preserved. The hysteresis loops at a higher relative pressure ($0.7 < P/P_0 < 1.0$) suggest the existence of inter-crystalline mesopores produced by the stacking of nano-sized crystals [7,25], which is particularly evident in 10-ZSM-5-80 (Fig. 2j). This result is consistent with the loosely stacked primary nanocrystals in SEM and TEM images (Fig. 2c and g). The pore size distribution in Fig. 2k further demonstrates the presence of mesopores (4–25 nm) in 10-ZSM-5-80. The BET parameters calculated from BJH model is showed in Table 1. The external surface area of 10-ZSM-5-80 increases to $150 \text{ m}^2/\text{g}$ compared to that of 0-ZSM-5-80 ($55 \text{ m}^2/\text{g}$), 5-ZSM-5-80 ($78 \text{ m}^2/\text{g}$), and 20-ZSM-5-80 ($56 \text{ m}^2/\text{g}$). Meanwhile, the mesopore volume is also enhanced to $0.37 \text{ cm}^3/\text{g}$, which is 3 times higher than that of 0-ZSM-5-80 ($0.12 \text{ cm}^3/\text{g}$). Furthermore, the N_2 adsorption-desorption isotherms and pore size distributions of different Si/Al ratios with the addition of 10-NCF show little trend (Fig. S8). Meanwhile, the samples have similar specific surface area and pore volume (Table 1), indicating that the variation of aluminum content has little effect on the pore structure of ZSM-5 zeolite.

The acidity of the zeolites is evaluated by NH_3 -TPD (Fig. 2l and Fig. S9), and the detailed acidity distribution is summarized in Table 2. All the zeolite samples exhibit two distinct desorption peaks at around $125\text{--}145^\circ\text{C}$ and $390\text{--}425^\circ\text{C}$, symbolizing desorbed NH_3 from weak and strong acid sites, respectively [26]. With decreasing Si/Al ratio, the total acidity of 10-ZSM-5- y ($y = 40, 80, 100$, and 150) gradually increase from $655 \text{ }\mu\text{mol/g}$ for 10-ZSM-5-150 to $950 \text{ }\mu\text{mol/g}$ for 10-ZSM-5-40. A similar variation trend is also observed for the weak and strong acidity of 10-ZSM-5- y series. This is consistent with previous reports that increasing Al content would result in higher acid site concentrations/intensities [27]. It is interesting to note that the acidity of zeolites varies with their morphologies, although the Si/Al ratio remain

Table 1
Porosity properties of all NCF-modified ZSM-5 zeolites.

Samples	Surface Area (m^2/g)			Pore Volume (cm^3/g)		
	Total	Micropore	Mesopore	Total	Micropore	Mesopore
0-ZSM-5-80	425	370	55	0.31	0.19	0.12
5-ZSM-5-80	431	353	78	0.31	0.16	0.15
10-ZSM-5-80	453	303	150	0.49	0.12	0.37
20-ZSM-5-80	420	364	56	0.29	0.17	0.12
10-ZSM-5-40	460	308	152	0.51	0.13	0.38
10-ZSM-5-100	436	306	130	0.44	0.13	0.31
10-ZSM-5-150	427	302	125	0.43	0.13	0.30

Table 2
Acidity distribution of all NCF-modified ZSM-5 zeolites.

Samples	Amount ($\mu\text{mol/g-NH}_3$)		Total amount ($\mu\text{mol/g}$)	Temperature ($^\circ\text{C}$)	
	Weak acid sites	Strong acid sites	Total acid sites	Weak acid sites	Strong acid sites
0-ZSM-5-80	691	135	826	138	420
5-ZSM-5-80	652	124	776	137	414
10-ZSM-5-80	646	119	765	137	414
20-ZSM-5-80	655	125	780	137	415
10-ZSM-5-40	753	190	943	140	423
10-ZSM-5-100	623	101	724	134	406
10-ZSM-5-150	599	46	645	130	395

the same. Table 2 intuitively displays that the hierarchical ZSM-5 has a much smaller total acid amount than the corresponding microporous zeolite, for example, 10-ZSM-5-80 has a total acid amount of $765 \text{ }\mu\text{mol/g}$, $61 \text{ }\mu\text{mol/g}$ less than the $826 \text{ }\mu\text{mol/g}$ of the corresponding 0-ZSM-5-80. Lower acid amount in hierarchical 10-ZSM-5-80 can be ascribed to the weakened microporous area as shown in Table 1 [28,29].

3.3. Effects of inter-crystalline mesopores on the mild conversion of glucose

Since catalytic reactions often occur at the internal active sites of the zeolite, the deoxygenation of active oxygenation intermediates highly depends on the diffusion of into the zeolite pores, whose structures strongly affect the bio-oil composition based on the reactant, product, and transition-state shape selectivity. To illustrate the structural advantages of nano-sized ZSM-5 with inter-crystalline mesopores for bio-oil production, ZSM-5 zeolites with a similar Si/Al ratio of 80 but different NCF additions (denoted as x -ZSM-5-80 ($x = 0, 5, 10$, and 20)) were synthesized and tested for low-temperature conversion of glucose. The product distribution, selectivity, and carbon distributions of aromatics are depicted in Fig. 3. As expected, the solid yield decreased in the order of 0-ZSM-5-80 (37.1 wt\%) > 20-ZSM-5-80 (35.6 wt\%) > 5-ZSM-5-80 (35.1 wt\%) > 10-ZSM-5-80 (24.7 wt\%), and liquid yield continuously increased from 35.0 wt\% for 0-ZSM-5-80– 47.3 wt\% for 10-ZSM-5-80 and then decreased to 38.4 wt\% for 20-ZSM-5-80 (Fig. 3a). The outstanding results obtained by 10-ZSM-5-80 benefits from the introduced inter-crystalline mesopores, which enhance molecular diffusion and inhibit their repolymerization to coke [30]. The gas yield ranged from 24.0 vol\% to 28.0 vol\% with little variation.

The composition of the gas obtained by the different mesoporosities series was depicted in Fig. 3b. The mesoporous structure was more conducive to deoxygenation, which can be confirmed by a maximum CO (49.5 vol\%) and CO_2 (48.5 vol\%) selectivity of 10-ZSM-5-80. In addition, CO selectivity was higher than CO_2 , suggesting that the catalytic decarbonylation reaction to CO was more active than decarboxylation reaction to CO_2 [31].

The composition of the bio-oil is shown in Fig. 3c. Due to the complexity of liquid oil, its composition in this work is categorized into aromatic hydrocarbons (e.g., MAHs and PAHs), oxygenates and others for better analysis. Compared with 0-ZSM-5-80, mesoporous x -ZSM-5-80 ($x = 5, 10, 20$) improved the quality of liquid oil by promoting the conversion of oxygenates to aromatic hydrocarbons. Specifically, with increasing NCF addition, the selectivity of oxygenates decreased from 14.6 area\% for 0-ZSM-5-80– 2.5 area\% for 10-ZSM-5-80 and then increased to 14.3 area\% for 20-ZSM-5-80, while the selectivity of aromatic hydrocarbons changed in the opposite sequence, that is, increased

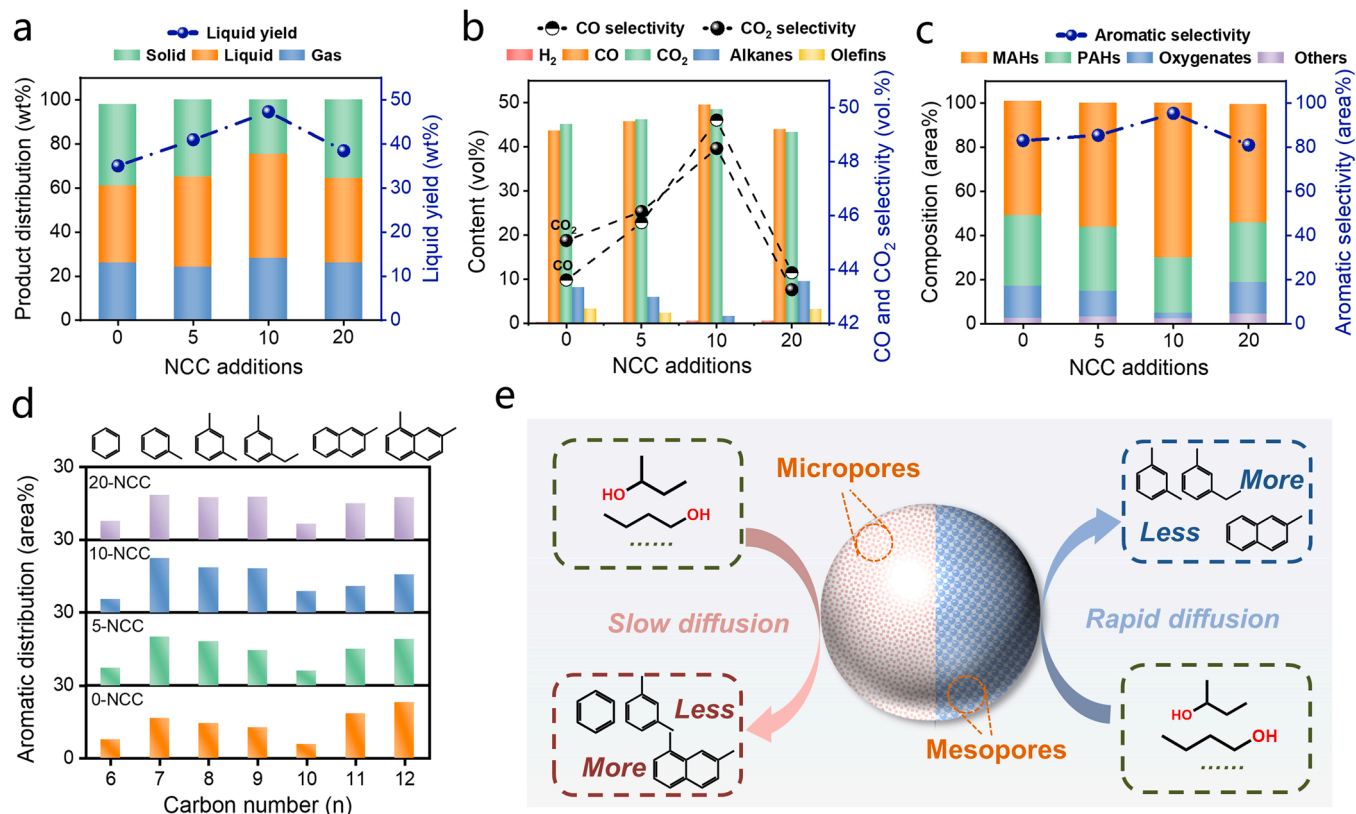


Fig. 3. Effects of inter-crystalline mesopores on the (a) product distribution, (b) gaseous composition and selectivity, (c) bio-oil composition and selectivity, (d) aromatics distribution on carbon number. (e) Schematic of the effect of zeolite mesoporosity on product selectivity.

from 83.0 area% for 0-ZSM-5-80–95.4 area% for 10-ZSM-5-80 and then decreased to 81.0 area% for 20-ZSM-5-80. This phenomenon can be explained by the more exposed acid sites on the nano-sized 10-ZSM-5-80 with inter-crystalline mesopores, thus facilitating the deoxygenation of oxygenates into aromatic hydrocarbons [28,32]. MAHs, especially BTEX, have a wide range of applications in petroleum processing and other fields and constitute the major market for aromatics. As shown in Fig. 3d, the carbon numbers of the aromatic hydrocarbons are mainly distributed in two intervals, namely C_6 – C_{10} (MAHs), and C_{11} – C_{12+} (PAHs), respectively. The selectivity of MAHs increased significantly from 49.9 area% for 0-ZSM-5-80–70.2 area% for 10-ZSM-5-80, and then decreased to 53.8 area% for 20-ZSM-5-80. This is because 0-ZSM-5-80 with well-defined micropores and higher acid strength would severely restrict the diffusion of MAHs from micropores to the external surface. These MAHs may polymerize within the micropores to form PAHs, which then lead to the rapid catalyst deactivation due to the coverage on strong acid sites and blocking of micropores (Fig. 3e). This is consistent with the maximum PAHs selectivity of 33.0 area% for 0-ZSM-5-80, which has the largest micropore area. Thus, a suitable mesoporous diffusion channel is required for glucose conversion to produce MAHs.

3.4. Effects of acidity on the mild conversion of glucose

The catalytic activity of 10-ZSM-5- y ($y = 40, 80, 100$, and 150) was also investigated in the low-temperature conversion of glucose, aiming to build the relationship between zeolite acidity and aromatics selectivity. Fig. 4a shows the product distribution obtained by 10-ZSM-5 with various acidities. With the increase in acidity, the liquid oil yield gradually increased from 29.1 wt% for 10-ZSM-5-150 to 47.3 wt% for 10-ZSM-5-80, whereas a further increase in acidity decreased the value to 36.7 wt% for 10-ZSM-5-40. Such a variation trend is opposite to the gas yield, which first decreased from 42 wt% for 10-ZSM-5-150 to 28 wt%

for 10-ZSM-5-80 and then increased to 30 wt% for 10-ZSM-5-40. According to the distribution of acid sites summarized in Table 2, it can be explained that moderate acid strength is favorable for converting the glucose into liquid products, whereas an excessive acidity would strengthen the secondary cracking of intermediates into non-condensable gases (e.g., CO_2 , CO, CH_4) [7,25,33].

Fig. 4b displays the gas composition obtained by various Si/Al ratios. Carbon oxides (CO_x), consisting of CO and CO_2 , are the major permanent gas products, with a selectivity larger than 95 vol%. This can be attributed to the thermal decomposition of carboxylic and carbonyl functional groups or the abscission of C–O bonds along with the generation of condensable oxygenates [34]. With the increase of Si/Al ratios, the selectivity of CO first increased and then decreased while the selectivity of CO_2 showed an opposite trend, and the maximum CO generation was achieved by 10-ZSM-5-80. The variations in CO/ CO_2 represents the degree of decarbonylation/decarboxylation of oxygenates [35]. The decarboxylation reaction occurred mainly during the conversion of glucose to intermediates. The presence of moderate acidity zeolite accelerated the intermediate to produce more CO by decarbonylation reaction, which leads to further conversion to aromatics [36,37]. Therefore, it is reasonable to speculate that there is a positive correlation between the formation of CO by decarbonylation and the generation of aromatics during the low-temperature conversion of glucose.

The composition of the liquid oil obtained from the 10-ZSM-5 series is depicted in Fig. 4c. In addition, the effect of the acidity and type of acid sites on the liquid oil selectivity is further analyzed. The strong acidity facilitates the formation of aromatics by promoting a series of reactions (e.g. decarboxylation, decarbonization, cyclization, etc.) of oxygen-containing intermediates on the acidic sites of the catalyst [38, 39]. Especially, the Lewis acid sites (LASs) plays an important role in deoxygenation process, the extent of deoxygenation increases with the concentration of LASs [40,41]. Thus, 10-ZSM-5- y series with more LASs (Fig. S10) gradually reduce the selectivity of oxygenates from 10.4 area

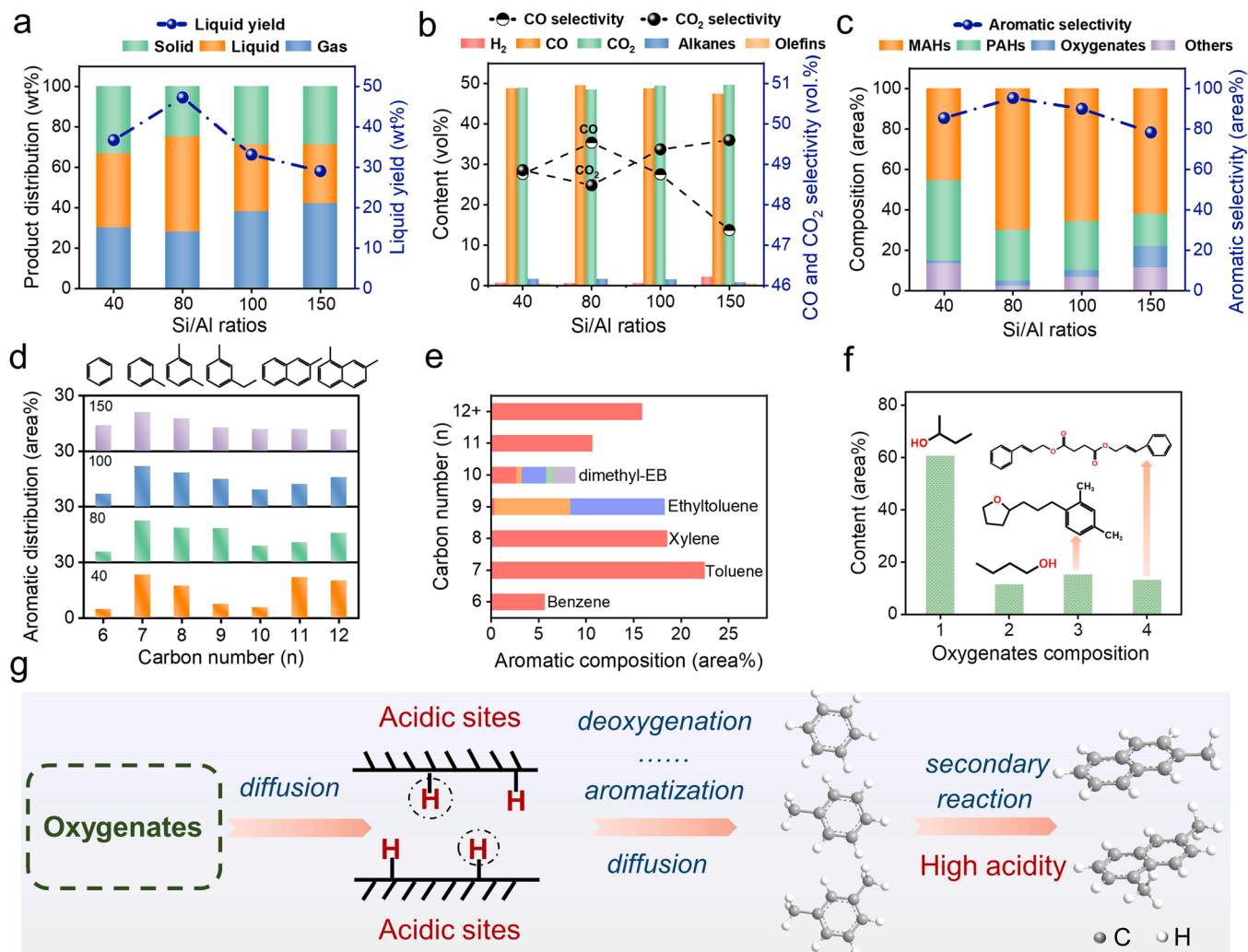


Fig. 4. Effects of acidity on the (a) product distribution, (b) gaseous composition and selectivity, (c) bio-oil composition and selectivity, (d) aromatics distribution on carbon number. (e) Aromatics composition and (f) oxygenates composition over 10-ZSM-5-80 catalyst. (g) Schematic of the effect of zeolite acidity on product selectivity.

% for 10-ZSM-5-150 to 1.2 area% for 10-ZSM-5-40. In addition, the Brønsted acid sites (BASs) are essential in aromatization reactions, where aromatics are produced by olefin cyclization and hydrogen transfer, and BASs facilitate the processes of cyclization and hydrogen transfer [42,43]. However, the maximum MAHs selectivity was obtained by 10-ZSM-5-80 (70.2 area%, Fig. S11 and Table S2) rather than 10-ZSM-5-40 (45.6 area%). This can be explained by the fact that excess concentration of BASs in zeolite channels could strongly adsorb MAHs molecules and restrict their diffusion out, which in turn promotes their repolymerization into PAHs, a precursor of coke [7,25,44]. This conclusion is also confirmed by the highest solid yield of 10-ZSM-5-40 (33.3 wt%) (Fig. 4a).

After analyzing the carbon distribution of aromatics, it was found that the highest proportion of C₆ (benzene) and the lower fraction of C₇-C₉ alkyl aromatics were obtained by 10-ZSM-5-150 (Fig. 4d), indicating that a weaker acidity is less capable for alkylation reaction [25,45]. The product distribution shifted to the aromatic hydrocarbons of C₇-C₉ with 10-ZSM-5-80, it may be related to the promotion of hydrogen transfer reaction by suitable acidity, which met the requirement for the alkylation reaction [28]. Additionally, the proportion of heavy aromatics (C₁₁-C₁₂+) gradually increased with the strengthened acidity, which was consistent with previous report that excessive zeolite acidity prompts the repolymerization of MAHs to PAHs. The composition of aromatics from 10-ZSM-5-80 is presented in Fig. 4e. The aromatic hydrocarbons

were mainly distributed in C₇-C₉ (59.1%), and the main products were toluene, xylene, and 3-ethyltoluene. Besides, the oxygenate composition obtained by 10-ZSM-5-80 was also analyzed (Fig. 4f). The oxygenates were mainly alcohols, and the selectivity of oxygenates in liquid was only 2.5 area% (Fig. 4c). Compared with catalytic fast pyrolysis, almost no furan was detected in the low-temperature melting-catalysis strategy, thus inhibiting the coke deposition and promoting the continuous deoxygenation of the intermediates to aromatics (Fig. S12). Therefore, in order to avoid the occurrence of secondary reactions in excessive acidity, a reasonable control of acidity is more favorable for the diffusion of reaction intermediates to zeolite acidic sites for a series of reactions to form MAHs (Fig. 4g).

3.5. Online products evolution analysis

To acquire deeper insight into the mechanism, TG-DSC and TG-FTIR-MS coupling system was employed to investigate the reaction process. TG connected with FTIR was conducted for online monitoring of gaseous products and functional groups. The peak upward in DSC curve indicates an exothermic process, while the peak downward represents an endothermic process.

Three main weight loss stages can be observed in TG-DTG curves (Fig. 5a). The initial mass loss occurs between ambient temperature and 130 °C, and the mass loss in this region is about 3.1 wt%, also depicted

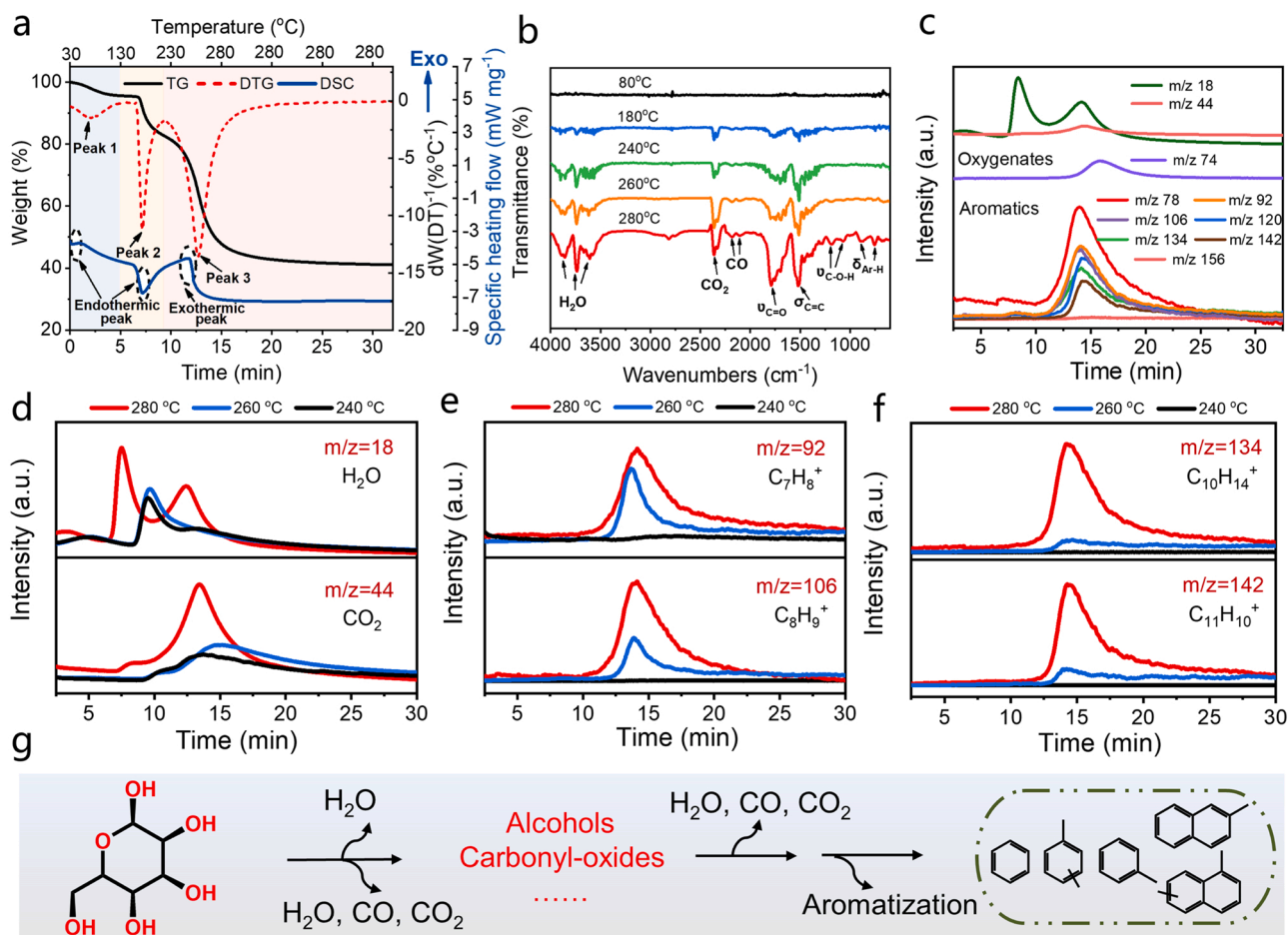


Fig. 5. TG-DSC and TG-FTIR-MS analyses over a 10-ZSM-5-80 catalyst (a) TG analysis curve, DTG curve, and DSC curve of the glucose. (b) FTIR spectra of the gaseous products at the maximum decomposition rate (80, 180, and 280 °C) and specific temperatures (240 and 260 °C). (c) The ion fragments of main gaseous products in the MS analysis. Ion abundance distributions of some specific gas fragments at different temperatures of (d) $m/z = 18$ (H₂O), $m/z = 44$ (CO₂), (e) $m/z = 92$ (C₇H₈⁺), $m/z = 106$ (C₈H₉⁺), (f) $m/z = 134$ (C₁₀H₁₄⁺), $m/z = 142$ (C₁₁H₁₀⁺). (g) Proposed reaction pathways in three weight loss stages.

by a small peak (peak 1) in the DTG curves. The slight weight loss is caused by the volatilization of free and bound water in samples, as confirmed by the endothermic peak in DSC (Fig. 5a) and weaker H₂O signals in FTIR spectrum (black line in Fig. 5b). The presence of H₂O may be the result of outgassing of the free water simply absorbed in zeolite catalyst, which was known to be hygroscopic [46,47].

After evaporation of moisture, some light volatiles are expected to be released within the temperature of 130–220 °C with a mass loss of ~12 wt%. The chemical structure of glucose starts to decompose and soften. The endothermic peak at ~150 °C is assigned to the melting of glucose [48]. Blue line in Fig. 5b shows the FTIR spectrum of the gas products at temperature corresponding to the maximum DTG (~180 °C). The hydroxyl groups spectrum band (4000–3600 cm⁻¹) indicates the formation of H₂O, which is produced by the dehydration of the oxygen-containing groups of glucose. The characteristic “w” shape absorption peaks at 2360 cm⁻¹ and 2340 cm⁻¹ refer to the CO₂ asymmetric stretching vibration. The weaker C≡O stretching vibration absorption peak in the range of 2270–1980 cm⁻¹ indicates the existence of CO in the gaseous products. C=O stretching vibrational band at 1780 cm⁻¹ is also observed. At lower temperature, carbonyl and carbon oxygen bond with poor thermal stability could break down and recombine, which promotes the production of CO and CO₂ [49]. Thus, the molten glucose may first undergo C-C and C-O bond cleavage by 10-ZSM-5-80 to produce non-condensable gas and small oxygenate intermediates.

Notably, the third stage from 220 to 280 °C is the most weight loss

stage among the three, and the weight loss rate is 48.8 wt%. It can be found that the FTIR spectrum of the third stage is much more complicated than the second stage (Fig. 5b). The absorption peak at 1520 cm⁻¹ is the C=C backbone stretching vibration on the benzene ring. The bands at 680–880 cm⁻¹ represents aromatic C-H out-of-plane bending vibration [50], indicating the formation of substituted benzene rings, especially mono- and 1,3-disubstituted aromatics. The absorption band at 1200–1050 cm⁻¹ and 1780 cm⁻¹ are assigned to the stretching vibration of C-O-H and C=O, respectively, suggesting the presence of oxygenates (e.g., alcohols, aldehydes, and ketones). In addition, the generation of small molecule gaseous products such as CO, CO₂, and H₂O can also be observed. Therefore, the third stage mainly include deoxygenation and aromatization process, which is further confirmed by the presence of a distinct exothermic peak in this temperature range (Fig. 5a).

Coupled online mass is used as a complementary tool to follow the evolutions of the mass in parallel, depending on the temperature and the chemical composition of the released vapors. The profiles of the change in ion current as a function of time corresponding to the possible compounds based on the mass-to-ion ratio (m/z) and the NIST database are shown in Fig. 5c and Table S3. Large amount of CO₂ ($m/z = 44$) and H₂O ($m/z = 18$) are detected at the temperature range of 150–220 °C because of high content of hydroxyl groups and oxygen atoms present in glucose, confirming the decomposition of glucose into small molecule oxygenates. However, a continuous detection of water is observed during reaction. This is because if the output flow rate of the TGA is not

the same as the vacuum flow rate entering the MS, a small amount of ambient water might be captured by the highly vacuumed MS instrument due to the high ambient humidity, leading to a continual detection of water by MS. The m/z of the fragments is mainly distributed between 74 and 156 at a higher temperature, which is associated with the formation of oxygenates and aromatics. The ionic fragment with m/z of 74 corresponds to the presence of $C_4H_{10}O^+$ and $C_3H_6O_2^+$, as evidenced by the C-O-H and C=O stretching vibrations in Fig. 5b. The m/z of 78, 92, 106, 120, 134, 142 and 156 represent the characteristic ions ($C_6H_5^+$, $C_7H_8^+$, $C_8H_{10}^+$, $C_9H_{12}^+$, $C_{10}H_{14}^+$, $C_{11}H_{16}^+$ and $C_{12}H_{18}^+$) of aryl series ions [50]. It can be found that the differences in peak times of aromatic hydrocarbons are not significant, which further indicated that the zeolite catalysts had certain adsorption properties to MAHs [51] and reasonable control of the acidity of zeolites is essential. At the same time, oxygen-containing gases such as CO_2 could still be detected, indicating that the aromatization stage is accompanied by deoxygenation reaction.

A further attempt was made by studying the influence of temperature on the aromatization stage. The catalytic experiments were conducted at 240, 260, and 280 °C, respectively, and the results were combined with TG-FTIR-MS coupling analysis. Fig. 5d shows the evolution of H_2O and CO_2 at different temperatures. The two mass spectral signals correspond to the DTG peaks indicate that both the glucose pre-decomposition and aromatization stages involved dehydration and decarboxylation processes [52]. The signal strengths of H_2O and CO_2 were weaker at 260 and 240 °C compared to 280 °C, indicating that higher temperature favor the cleavage of C-C and C-O bonds. The signal peaks of the aromatic ion fragments are shown in Fig. 5e and f. At 240 °C, the signal of aromatic ionic fragments is barely detectable, which is consistent with the absence of C=C backbone stretching vibration in FTIR and undetectable aromatic compositions in the liquid oil (Fig. S13). As the temperature increases, the $C_7H_8^+$, $C_8H_{10}^+$, $C_{10}H_{14}^+$ and $C_{11}H_{16}^+$ signals become stronger, indicating that higher temperature facilitates the conversion of oxygenate intermediates to aromatics by ZSM-5 zeolite. This is also evidenced by the deepened dehydration, decarboxylation and decarbonylation as the reaction proceeds (Fig. 5b). As a result, under mild conditions, glucose undergone three main stages of dehydration,

decarbonylation and aromatization to produce aromatic hydrocarbons (Fig. 5g).

3.6. Mechanism investigation

Since the kinetic diameter of glucose (~ 8.50 Å) is significantly larger than the micropore size of ZSM-5 (~ 5.50 Å), it cannot diffuse directly into the micropores before decomposition. Based on this, a possible reaction mechanism for the low-temperature conversion of glucose to value-added MAHs by hierarchical ZSM-5 zeolite is proposed in Fig. 6. The conversion process should start with the glucose melting (~ 150 °C) and flowing to access the zeolite crystals to start the reaction, which might be partially confirmed by the fact that the catalytic results were less vulnerable to the mixing manner of glucose and catalyst (Fig. S14). Subsequent cascade reactions proceed in multiple steps, including primary cracking of “molten glucose” into oxygenate intermediates (e.g., alcohols, aldehydes, and ketones etc.), and then these oxygenate intermediates with appropriate molecule sizes diffused into the ZSM-5 micropores and underwent a series of deoxygenation reactions, especially decarbonylation. This is because the decarbonylation of oxygenates is the source of olefins that constitute the “hydrocarbon pool” [53]. Finally, oligomerization, cyclization, and aromatization reactions took place in the “hydrocarbon pool” to produce aromatic hydrocarbons, especially the MAHs, which subsequently diffused out from the ordered-connected mesopores and collected in the liquid oil. It should be noted that the diffusion of these intermediates and MAHs within micropores is relatively slow, whereas microporous channel utilization and acidic site accessibility are significantly promoted by benefiting from the enhanced mass transfer through inter-crystalline mesopores. This might explain the limited oxygenates in the product of 10-ZSM-5-80 and many coke formation in microporous ZSM-5. In addition, the excellent regenerative catalytic activity and structural integrity of 10-ZSM-5-80 make it an effective reference for the conversion of biomass to aromatics under mild conditions (Text S1, Fig. S15 and Table S5).

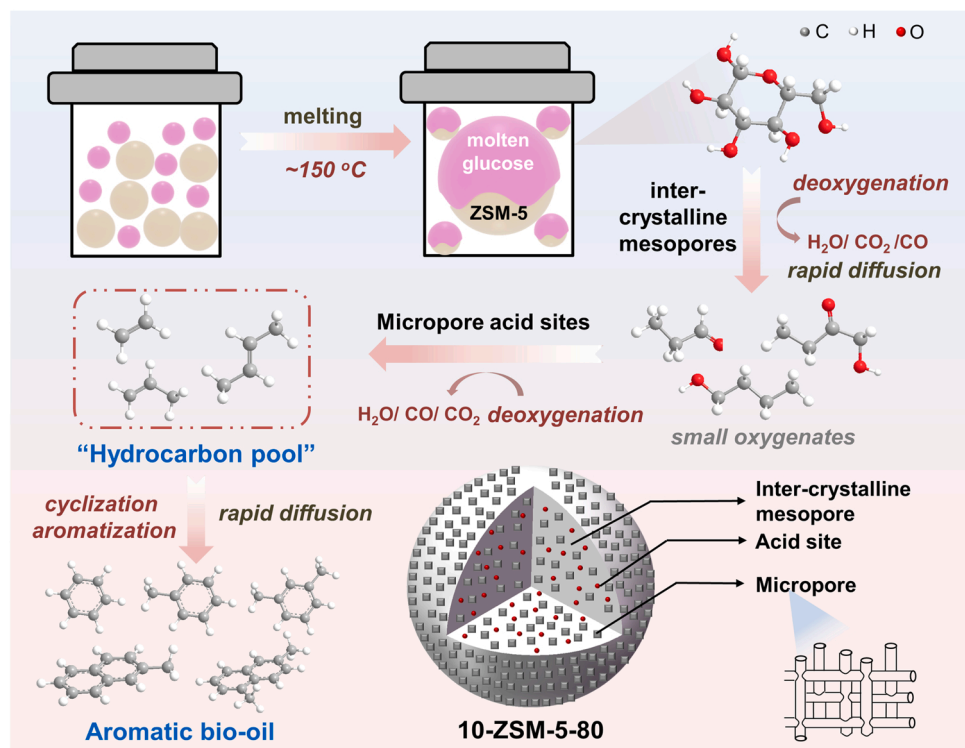


Fig. 6. Proposed reaction mechanism for the low-temperature conversion of glucose over nano-sized mesoporous 10-ZSM-5-80.

4. Conclusions

In summary, we developed a novel melting-catalysis strategy to upgrade glucose into value-added aromatics by nano-sized mesoporous ZSM-5 catalyst at a low temperature of 280 °C and without external H₂ input. We demonstrated the phase change of the reactant from solid to liquid by melting promotes accessibility to catalytic sites so as to enhance subsequent catalytic processes. The results revealed that the aromatics production and selectivity are affected by the zeolite porosity and acidity. The inter-crystalline mesopores facilitate the diffusion of molten glucose and intermediates, improving the accessibility of interior acid sites. High acidity in micropores is beneficial for formation of aromatics, especially MAHs, whereas excessive acidity shows an adverse effect by promoting the repolymerization of MAHs into PAHs (a coke precursor). 10-ZSM-5-80 with both abundant inter-crystalline mesopores and moderate acid sites exhibits best performance in the conversion of glucose to aromatics under mild conditions, achieving an aromatics selectivity up to 95.4 area% with 70.2% of them being MAHs (C₆-C₁₀). TG-DSC and TG-FTIR-MS analysis bring insights into the product evolution process, that is, 1) it is the “molten glucose” rather than “glucose vapors” that is initially captured by the mesopores. 2) decomposition of glucose into small molecule oxygenate intermediates for diffusion into zeolite micropores with the release of CO₂ and H₂O between 130 and 220 °C, 3) formation of aromatics through deoxygenation and aromatization reactions above 260 °C. This work offers a novel and viable route to produce aromatics from renewable glucose carbohydrates under mild conditions, advancing the development of biomass utilization.

CRediT authorship contribution statement

Zhe Zhang: Investigation, Methodology, Software, Data curation, Original draft, **Huan Chen:** Investigation, Methodology, Software, Data curation, Formal analysis, Writing – review & editing, **Helin Pan:** Investigation, Formal analysis, **Dengle Duan:** Investigation, **Yayun Zhang:** Conceptualization, Formal analysis, Writing – review & editing, **Donghui Long:** Writing – review & editing.

Declaration of Competing Interest

The authors declare that they have no known competing financial interests or personal relationships that could have appeared to influence the work reported in this paper.

Data availability

Data will be made available on request.

Acknowledgements

This work was financially supported by National Natural Science Foundation of China (No. 22008073, No. 21878091), Shanghai Sailing Program (No. 20YF1410600), Fundamental Research Funds for the Central Universities, and Shanghai Talent Development Fund (No. 2021026).

Appendix A. Supporting information

Supplementary data associated with this article can be found in the online version at [doi:10.1016/j.apcatb.2022.122226](https://doi.org/10.1016/j.apcatb.2022.122226).

References

- [1] H. Chen, K. Wan, F. Zheng, Z. Zhang, Y. Zhang, D. Long, Mechanism insight into photocatalytic conversion of lignin for valuable chemicals and fuels production: a state-of-the-art review, *Renew. Sustain. Energy Rev.* 147 (2021), 111217, <https://doi.org/10.1016/j.rser.2021.111217>.
- [2] J. Liang, G. Shan, Y. Sun, Catalytic fast pyrolysis of lignocellulosic biomass: critical role of zeolite catalysts, *Renew. Sustain. Energy Rev.* 139 (2021), 110707, <https://doi.org/10.1016/j.rser.2021.110707>.
- [3] J. Zakzeski, P.C.A. Bruijninx, A.L. Jongerius, B.M. Weckhuysen, The catalytic valorization of lignin for the production of renewable chemicals, *Chem. Rev.* 110 (2010) 3552–3599, <https://doi.org/10.1021/cr900354u>.
- [4] M. Qian, H. Lei, Y. Zhao, E. Villota, E. Huo, C. Wang, X. Zhang, Lignin-mediated preparation of hierarchical ZSM-5 catalysts and their effects in the catalytic co-pyrolysis of softwood biomass and low-density polyethylene mixtures, *ACS Sustain. Chem. Eng.* 9 (2021) 12602–12613, <https://doi.org/10.1021/acssuschemeng.1c03863>.
- [5] C. Dorado, C.A. Mullen, A.A. Boateng, Origin of carbon in aromatic and olefin products derived from HZSM-5 catalyzed co-pyrolysis of cellulose and plastics via isotopic labeling, *Appl. Catal. B Environ.* 162 (2015) 338–345, <https://doi.org/10.1016/j.apcatb.2014.07.006>.
- [6] M. Yang, J. Shao, H. Yang, K. Zeng, Z. Wu, Y. Chen, X. Bai, H. Chen, Enhancing the production of light olefins and aromatics from catalytic fast pyrolysis of cellulose in a dual-catalyst fixed bed reactor, *Bioresour. Technol.* 273 (2019) 77–85, <https://doi.org/10.1016/j.biortech.2018.11.005>.
- [7] L. Wu, J. Xin, D. Xia, J. Sun, J. Liang, Enhanced production of hydrocarbons from the catalytic pyrolysis of maize straw over hierarchical ZSM-11 zeolites, *Appl. Catal. B Environ.* 317 (2022), 121775, <https://doi.org/10.1016/j.apcatb.2022.121775>.
- [8] T.R. Carlson, J. Jae, Y.-C. Lin, G.A. Tompsett, G.W. Huber, Catalytic fast pyrolysis of glucose with HZSM-5: The combined homogeneous and heterogeneous reactions, *J. Catal.* 270 (2010) 110–124, <https://doi.org/10.1016/j.jcat.2009.12.013>.
- [9] K. Wang, K.H. Kim, R.C. Brown, Catalytic pyrolysis of individual components of lignocellulosic biomass, *Green. Chem.* 16 (2014) 727–735, <https://doi.org/10.1039/C3GC41288A>.
- [10] X. Xue, L. Wu, X. Wei, J. Liang, Y. Sun, Product modification in catalytic fast pyrolysis of corn stalk: the decoupled effect of acidity and porosity within a core-shell micro-/mesoporous zeolite, *ACS Sustain. Chem. Eng.* 8 (2020) 7445–7453, <https://doi.org/10.1021/acssuschemeng.0c01518>.
- [11] V.N. Kalekar, P.D. Vaidya, Hydrogen production by aqueous-phase reforming of model compounds of wet biomass over platinum catalysts, *Ind. Eng. Chem. Res.* 61 (2022) 10004–10013, <https://doi.org/10.1021/acs.iecr.2c01131>.
- [12] F.A. Agblevor, H. Jahromi, Aqueous-phase synthesis of hydrocarbons from furfural reactions with low-molecular-weight biomass oxygenates, *Energy Fuels* 32 (2018) 8552–8562, <https://doi.org/10.1021/acs.energyfuels.8b02002>.
- [13] B. Meryemoglu, B. Kaya, S. Irmak, A. Hesenov, O. Erbatur, Comparison of batch aqueous-phase reforming of glycerol and lignocellulosic biomass hydrolysate, *Fuel* 97 (2012) 241–244, <https://doi.org/10.1016/j.fuel.2012.02.011>.
- [14] L. Dong, L. Lin, X. Han, X. Si, X. Liu, Y. Guo, F. Lu, S. Rudić, S.F. Parker, S. Yang, Y. Wang, Breaking the limit of lignin monomer production via cleavage of interunit carbon-carbon linkages, *Chem* 5 (2019) 1521–1536, <https://doi.org/10.1016/j.chempr.2019.03.007>.
- [15] Y. Zhang, D. Duan, H. Lei, E. Villota, R. Ruan, Jet fuel production from waste plastics via catalytic pyrolysis with activated carbons, *Appl. Energy* 251 (2019), 113337, <https://doi.org/10.1016/j.apenergy.2019.113337>.
- [16] Y. Chi, J. Xue, J. Zhuo, D. Zhang, M. Liu, Q. Yao, Catalytic co-pyrolysis of cellulose and polypropylene over all-silica mesoporous catalyst MCM-41 and Al-MCM-41, *Sci. Total Environ.* 633 (2018) 1105–1113, <https://doi.org/10.1016/j.scitotenv.2018.03.239>.
- [17] G.W. Huber, S. Iborra, A. Corma, Synthesis of transportation fuels from biomass: chemistry, catalysts, and engineering, *Chem. Rev.* 106 (2006) 4044–4098, <https://doi.org/10.1021/cr068360d>.
- [18] X. Zhang, Q. Chen, Q. Zhang, C. Wang, L. Ma, Y. Xu, Conversion of pyrolytic lignin to aromatic hydrocarbons by hydrocracking over pristine MoO₃ catalyst, *J. Anal. Appl. Pyrolysis* 135 (2018) 60–66, <https://doi.org/10.1016/j.jaap.2018.09.020>.
- [19] Q. Che, W. Yi, Y. Liu, X. Wang, H. Yang, H. Chen, Effect of mesopores in ZSM-5 on the catalytic conversion of acetic acid, furfural, and guaiacol, *Energy Fuels* 35 (2021) 6022–6029, <https://doi.org/10.1021/acs.energyfuels.0c04415>.
- [20] L.Y. Jia, M. Raad, S. Hamieh, J. Toufaily, T. Hamieh, M.M. Bettahar, G. Mauviel, M. Tarrighi, L. Pinard, A. Dufour, Catalytic fast pyrolysis of biomass: superior selectivity of hierarchical zeolites to aromatics, *Green. Chem.* 19 (2017) 5442–5459, <https://doi.org/10.1039/C7GC02309J>.
- [21] Y. Liao, R. Zhong, M. d'Halluin, D. Verboekend, B.F. Sels, Aromatics production from lignocellulosic biomass: shape selective dealkylation of lignin-derived phenolics over hierarchical ZSM-5, *ACS Sustain. Chem. Eng.* 8 (2020) 8713–8722, <https://doi.org/10.1021/acssuschemeng.0c02370>.
- [22] T. Fu, J. Chang, J. Shao, Z. Li, Fabrication of a nano-sized ZSM-5 zeolite with intercrystalline mesopores for conversion of methanol to gasoline, *J. Energy Chem.* 26 (2017) 139–146, <https://doi.org/10.1016/j.jechem.2016.09.011>.
- [23] J.A. Botas, D.P. Serrano, A. García, R. Ramos, Catalytic conversion of rapeseed oil for the production of raw chemicals, fuels and carbon nanotubes over Ni-modified nanocrystalline and hierarchical ZSM-5, *Appl. Catal. B Environ.* 145 (2014) 205–215, <https://doi.org/10.1016/j.apcatb.2012.12.023>.
- [24] X.-Y. Ren, J.-P. Cao, X.-Y. Zhao, Z. Yang, Y.-J. Wang, Q. Chen, M. Zhao, X.-Y. Wei, Catalytic conversion of lignite pyrolysis volatiles to light aromatics over ZSM-5: SiO₂/Al₂O₃ ratio effects and mechanism insights, *J. Anal. Appl. Pyrolysis* 139 (2019) 22–30, <https://doi.org/10.1016/j.jaap.2019.01.003>.
- [25] L. Wu, J. Zhang, X. Xue, J. Liang, Y. Sun, Hydrocarbon-rich bio-oil production from catalytic pyrolysis of biomass over the undervalued ZSM-11 zeolites, *ACS EST Eng.* 2 (2022) 670–680, <https://doi.org/10.1021/acsesteng.1c00329>.

- [26] W. Dai, L. Zhang, R. Liu, G. Wu, N. Guan, L. Li, Plate-like ZSM-5 zeolites as robust catalysts for the cracking of hydrocarbons, *ACS Appl. Mater. Interfaces* 14 (2022) 11415–11424, <https://doi.org/10.1021/acsami.1c23614>.
- [27] H. Pan, Q. Pan, Y. Zhao, Y. Luo, X. Shu, M. He, A green and efficient synthesis of ZSM-5 using NaY as seed with mother liquid recycling and in the absence of organic template, *Ind. Eng. Chem. Res.* 49 (2010) 7294–7302, <https://doi.org/10.1021/ie100191a>.
- [28] C. Zhu, D.P. Gamliel, J.A. Valla, G.M. Bollas, Fischer-tropsch synthesis in monolith catalysts coated with hierarchical ZSM-5, *Appl. Catal. B Environ.* 284 (2021), 119719, <https://doi.org/10.1016/j.apcatb.2020.119719>.
- [29] L. Zhang, X. Sun, M. Pan, X. Yang, Y. Liu, J. Sun, Q. Wang, J. Zheng, Y. Wang, J. Ma, W. Li, R. Li, Interfacial effects between carbon nanotube templates and precursors on fabricating a wall-crystallized hierarchical pore system in zeolite crystals, *J. Mater. Sci.* 55 (2020) 10412–10426, <https://doi.org/10.1007/s10853-020-04708-1>.
- [30] L. Fan, P. Chen, Y. Zhang, S. Liu, Y. Liu, Y. Wang, L. Dai, R. Ruan, Fast microwave-assisted catalytic co-pyrolysis of lignin and low-density polyethylene with HZSM-5 and MgO for improved bio-oil yield and quality, *Bioresour. Technol.* 225 (2017) 199–205, <https://doi.org/10.1016/j.biortech.2016.11.072>.
- [31] J. Wang, B.-C. Lin, Q.-X. Huang, Z.-Y. Ma, Y. Chi, J.-H. Yan, Aromatic hydrocarbon production and catalyst regeneration in pyrolysis of oily sludge using ZSM-5 zeolites as catalysts, *Energy Fuels* 31 (2017) 11681–11689, <https://doi.org/10.1021/acs.energyfuels.7b01855>.
- [32] L. Qiang, L. Wen-zhi, Z. Dong, Z. Xi-feng, Analytical pyrolysis–gas chromatography/mass spectrometry (Py–GC/MS) of sawdust with Al/SBA-15 catalysts, *J. Anal. Appl. Pyrolysis* 84 (2009) 131–138, <https://doi.org/10.1016/j.jaap.2009.01.002>.
- [33] L. Wu, X. Xue, H. Yu, C. Zhang, X. Wei, J. Liang, Y. Sun, Catalytic pyrolysis of poplar sawdust: Excellent hydrocarbon selectivity and activity of hollow zeolites, *Bioresour. Technol.* 317 (2020), 123954, <https://doi.org/10.1016/j.biortech.2020.123954>.
- [34] Y.-T. Cheng, G.W. Huber, Chemistry of furan conversion into aromatics and olefins over HZSM-5: a model biomass conversion reaction, *ACS Catal.* 1 (2011) 611–628, <https://doi.org/10.1021/cs200103j>.
- [35] X.-Y. Ren, J.-P. Cao, X.-Y. Zhao, Z. Yang, T.-L. Liu, X. Fan, Y.-P. Zhao, X.-Y. Wei, Catalytic upgrading of pyrolysis vapors from lignite over mono/bimetal-loaded mesoporous HZSM-5, *Fuel* 218 (2018) 33–40, <https://doi.org/10.1016/j.fuel.2018.01.017>.
- [36] H. Ben, A.J. Ragauskas, Influence of Si/Al Ratio of ZSM-5 Zeolite on the Properties of Lignin Pyrolysis Products, *ACS Sustain. Chem. Eng.* 1 (2013) 316–324, <https://doi.org/10.1021/sc300074n>.
- [37] C. Zhang, J. Xing, L. Song, H. Xin, S. Lin, L. Xing, X. Li, Aqueous-phase hydrodeoxygenation of lignin monomer eugenol: Influence of Si/Al ratio of HZSM-5 on catalytic performances, *Catal. Today* 234 (2014) 145–152, <https://doi.org/10.1016/j.cattod.2014.01.021>.
- [38] G. Fogassy, N. Thegarid, Y. Schuurman, C. Mirodatos, From biomass to bio-gasoline by FCC co-processing: effect of feed composition and catalyst structure on product quality, *Energy Environ. Sci.* 4 (2011) 5068, <https://doi.org/10.1039/c1ee02012a>.
- [39] P. Noor, M. Khanmohammadi, B. Roozbehani, F. Yaripour, A. Bagheri Garmarudi, Introduction of table sugar as a soft second template in ZSM-5 nanocatalyst and its effect on product distribution and catalyst lifetime in methanol to gasoline conversion, *J. Energy Chem.* 27 (2018) 582–590, <https://doi.org/10.1016/j.jechem.2017.10.031>.
- [40] X. Yang, F. Wang, R. Wei, S. Li, Y. Wu, P. Shen, H. Wang, L. Gao, G. Xiao, Synergy effect between hierarchical structured and Sn-modified H[Sn, Al]ZSM-5 zeolites on the catalysts for glycerol aromatization, *Microporous Mesoporous Mater.* 257 (2018) 154–161, <https://doi.org/10.1016/j.micromeso.2017.08.039>.
- [41] A. Veses, B. Puértolas, J.M. López, M.S. Callén, B. Solsona, T. García, Promoting deoxygenation of bio-oil by metal-loaded hierarchical ZSM-5 zeolites, *ACS Sustain. Chem. Eng.* 4 (2016) 1653–1660, <https://doi.org/10.1021/acssuschemeng.5b01606>.
- [42] U.V. Mentzel, S. Shunmugavel, S.L. Hraby, C.H. Christensen, M.S. Holm, High yield of liquid range olefins obtained by converting *i*-propanol over zeolite H-ZSM-5, *J. Am. Chem. Soc.* 131 (2009) 17009–17013, <https://doi.org/10.1021/ja907692t>.
- [43] F. Zhou, Y. Gao, G. Wu, F. Ma, C. Liu, Improved catalytic performance and decreased coke formation in post-treated ZSM-5 zeolites for methanol aromatization, *Microporous Mesoporous Mater.* 240 (2017) 96–107, <https://doi.org/10.1016/j.micromeso.2016.11.014>.
- [44] C. Engtrakul, C. Mukarakate, A.K. Starace, K.A. Magrini, A.K. Rogers, M.M. Yung, Effect of ZSM-5 acidity on aromatic product selectivity during upgrading of pine pyrolysis vapors, *Catal. Today* 269 (2016) 175–181, <https://doi.org/10.1016/j.cattod.2015.10.032>.
- [45] L. Fan, P. Chen, N. Zhou, S. Liu, Y. Zhang, Y. Liu, Y. Wang, M.M. Omar, P. Peng, M. Addy, Y. Cheng, R. Ruan, In-situ and ex-situ catalytic upgrading of vapors from microwave-assisted pyrolysis of lignin, *Bioresour. Technol.* 247 (2018) 851–858, <https://doi.org/10.1016/j.biortech.2017.09.200>.
- [46] B.K. Bessire, S.A. Lahankar, T.K. Minton, Pyrolysis of phenolic impregnated carbon ablator (PICA), *ACS Appl. Mater. Interfaces* 7 (2015) 1383–1395, <https://doi.org/10.1021/am507816f>.
- [47] E. Garofalo, P. Scarfato, L. Di Maio, A. Protopapa, L. Incarnato, Zeolites as effective desiccants to solve hygroscopicity issue of post-consumer mixed recycled polyolefins, *J. Clean. Prod.* 295 (2021), 126379, <https://doi.org/10.1016/j.jclepro.2021.126379>.
- [48] M. Hajalilgol, B. Waymack, D. Kellogg, Low temperature formation of aromatic hydrocarbon from pyrolysis of cellulosic materials, (2001) 9.
- [49] S. Wang, Y. Tang, H.H. Schobert, Y. Guo, W. Gao, X. Lu, FTIR and simultaneous TG/MS/FTIR study of Late Permian coals from Southern China, *J. Anal. Appl. Pyrolysis* 100 (2013) 75–80, <https://doi.org/10.1016/j.jaap.2012.11.021>.
- [50] J. Yang, H. Chen, W. Zhao, J. Zhou, TG–FTIR–MS study of pyrolysis products evolving from peat, *J. Anal. Appl. Pyrolysis* 117 (2016) 296–309, <https://doi.org/10.1016/j.jaap.2015.11.002>.
- [51] B.-S. Kim, Y.-M. Kim, H.W. Lee, J. Jae, D.H. Kim, S.-C. Jung, C. Watanabe, Y.-K. Park, Catalytic coprolysis of cellulose and thermoplastics over HZSM-5 and HY, *ACS Sustain. Chem. Eng.* 4 (2016) 1354–1363, <https://doi.org/10.1021/acssuschemeng.5b01381>.
- [52] P.R. Patwardhan, D.L. Dalluge, B.H. Shanks, R.C. Brown, Distinguishing primary and secondary reactions of cellulose pyrolysis, *Bioresour. Technol.* 102 (2011) 5265–5269, <https://doi.org/10.1016/j.biortech.2011.02.018>.
- [53] C.A. Mullen, P.C. Tarves, A.A. Boateng, Role of potassium exchange in catalytic pyrolysis of biomass over ZSM-5: formation of alkyl phenols and furans, *ACS Sustain. Chem. Eng.* 5 (2017) 2154–2162, <https://doi.org/10.1021/acssuschemeng.6b02262>.